Ultrasonic friction modulating rings for endoscopes

By

J.L. Nieuwenhuis
4604091

in partial fulfilment of the requirements for the degree of

Master of Science
in Mechanical Engineering

at the Delft University of Technology,
to be defended publicly on Thursday December 7, 2023 at 9:00 AM.

Daily supervisor:	Ir. Mostafa A. Atalla,	TU Delft
Supervisor:	Dr. ir. Aimée Sakes,	TU Delft
	Dr. ir. Michaël Wiertlewski,	TU Delft
Thesis committee:	Dr. ir. Aimée Sakes,	TU Delft
	Dr. ir. Michaël Wiertlewski,	TU Delft
	Dr. ir. Mathias .P. Peirlinck,	TU Delft

This thesis is confidential and cannot be made public until December 31, 2025.

Ultrasonic friction modulating rings for endoscopes

J.L. Nieuwenhuis

Abstract— **An endoscopy is a medical procedure to study tissue inside the body by directly inserting the endoscope into the organ or vessel. In this research, the focus is on arterial and intestinal tissue. An endoscopy consists of two phases; the navigation phase where the endoscope is navigated through the body, and the operation phase where the operation is carried out. During the navigation phase, low friction between the endoscope and the tissue is desired, while during the operation phase, higher friction is desired to counteract the natural motion of the body. This paper proposes an ultrasonically vibrated ring that can control the frictional properties on demand to adapt to both phases through fluid film levitation. In this concept, multiple friction-modulating rings are placed along the length of the endoscope. This research aims to optimize the previous version of friction modulation through an ultrasonically vibrating ring. This paper consists of a review of the previous concept; and the design, characterization, and experimental verification of the new prototype. The new design is less complex, and smaller, features better waterproofing, and improved vibrational performance. LDV measurements of the new prototype show that the developed finite element model can be used to accurately predict the vibrational characteristics of the ring. The friction reduction performance is experimentally determined and shows that on hard substrates in both air and water, up to 90% of friction reduction can be achieved. On the soft substrates used in testing, up to 20% friction reduction can be achieved in air and 4% in water. The experimental testing of the prototype confirms that the concept can achieve fluid film levitation in both compressible and incompressible fluid environments and thereby validates the proof of concept.**

I. INTRODUCTION

An endoscopy is a medical procedure to study the inside of the body. In contrast to many other medical imaging techniques, endoscopes are directly inserted into the organ or cavity. An endoscope is typically a thin long flexible tube with a small camera and can be fitted with additional instruments for specific applications, such as forceps for biopsies, either with or without needles. Endoscopes are instruments that are often tailored to their specific application. A colonoscope, an endoscope used to study the colon is permitted be over $10\,\mathrm{mm}$ diameter and may feature foreceps and a camera. Catheters however, which are used in arteries and studies of the heart, are typically $2\,\mathrm{mm}$ in diameter and often do not feature a camera [1].

One of the difficulties of using an endoscope arises from the frictional interaction between the outer walls of the endoscope and the inner wall of the body. Low friction between the endoscope and the wall makes the navigation phase easier for the surgeon and reduces the strain on the tissue. Minimal friction between the endoscope and the vessel wall can be achieved, for example through the use of lubrication or a hydrophilic polymer surface [2], [3]. When the endoscope is in place, low friction makes the endoscope head unsteady and more likely to move relative to the vessel wall due to the natural motion of the body[4].

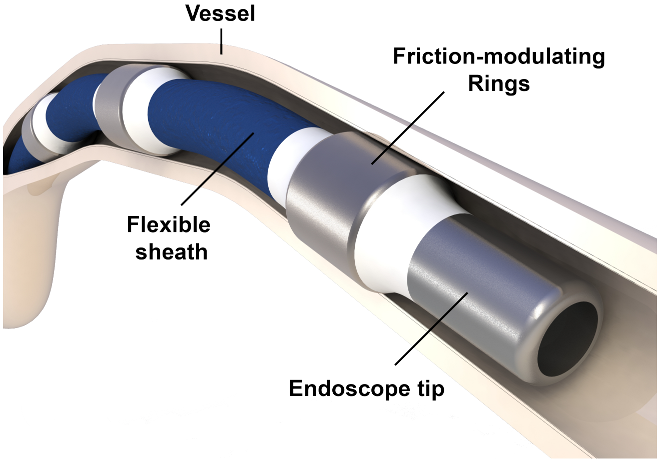

Fig. 1: An endoscope with friction modulation elements in a vessel.

A high frictional force between the endoscope and the vessel makes the operation phase more secure since the endoscope head is less likely to move unintentionally, but it also makes the navigation phase more difficult and increases the strain on the tissue [2]. These contradicting demands for either phase mean that with a constant friction coefficient, compromises will have to be made in terms of ease of insertion versus operational stability.

One solution is a low friction coating for the navigation phase, combined with a mechanism to stabilize the endoscope for the operation phase. Ali et al. [4] classified 13 mechanisms in their complete schematic overview of stabilizing mechanisms for catheters. The majority of these solutions are placed at the tip of the catheter, putting increased strain on the tissue. Examples of these mechanisms are balloon structures which can be inflated once in the area of interest and increase the holding capacity through an increased normal force. A downside of a balloon structure is that blood flow around the balloon is limited. Similarly, basket structures can be used that expand outwards and press against the vessel wall. One mechanism that is not outlined in the overview is the modulation of the friction coefficient between the endoscope and the vessel.

This research aims to design and test an active element that can be implemented in the endoscope which allows the frictional coefficient between the endoscope and the vessel wall to be actively controlled. The end goal of this research is to design a solution that is adaptable to a variety of endoscopes. The vision is that the friction modulation rings will be distributed along the length of the sheath of the endoscope. The sheath itself features a low-friction coating, which results in minimal friction along the entire

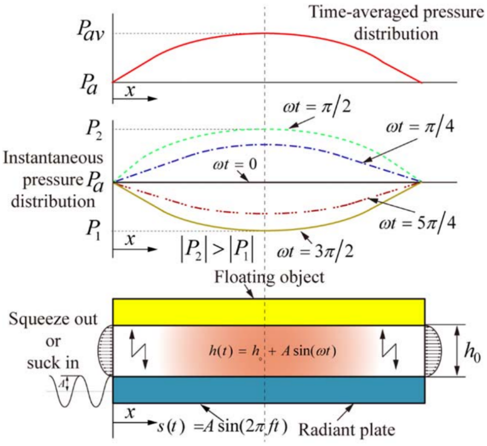

Fig. 2: A schematic representation of the squeeze film; The asymmetry of the compressible fluid results in a time-averaged positive pressure[6].

length of the endoscope when the friction reduction is active. The result of this is shown in figure 1. These rings can reduce the friction between the ring and the vessel during the navigational phase for easy insertion. Once the operation destination is reached, the friction reduction is disabled and the working end of the endoscope is securely kept in place without excessive strain on the tissue.

This active friction modulation will be achieved using fluid film levitation through the application of ultrasonic vibration. This vibration will be applied to the outer surface of the resonant element through piezoelectric elements which are actuated at the resonant frequency of the element. The goal of this research is to improve upon an earlier design made and studied by Jeroen Tuijp [5], and validate the friction-modulating effect of the concept.

This report starts with background information and explains which metrics will be used to describe and evaluate the designs. Followed by the evaluation of the previous design. After this, the new concept is shown and evaluated using the same metrics. After this, several prototypes of the new concept are made and various tests are conducted. Tests begin with frequency and amplitude response studies. After this experimental testing on various substrates in varying conditions is conducted.

II. BACKGROUND

A. The squeeze film

If two objects are in close proximity and one vibrates at a high frequency, a levitation layer is formed. In compressible fluid this phenomenon is referred to as a squeeze film. A schematic representation of the mechanism that induces a squeeze film is shown in figure 2.

The radiant plate is vibrated normally to the floating plate by means of a vibrational actuator. The upwards movement of the radiant plate pushes the air out from between the two plates and the downward movement sucks air back in. However, if the width of the film between the plates is far larger than the film height, the flow can be restricted. Then, and with a high vibration amplitude and frequency the air in the film can not flow in and out sufficiently quickly. Instead of this, the air in the film compresses and decompresses periodically. Due to the compressibility of the fluid, the magnitude of the positive pressure peak is larger than that of the negative pressure and thus the time-averaged pressure in the film is above ambient. This time-averaged positive pressure results in the levitation force. This levitation force partly replaces the contact force between the surfaces, effectively reducing the friction coefficient. This phenomenon occurs with air film thicknesses in the range of several tens of microns, at vibration amplitudes of 1-2 microns and frequencies over 20 kHz [7].

The squeeze film effect has already been successfully implemented in many applications [8], [9], [10], [11], [12], [6], [13], [14]. In many of these research papers air is used as the squeeze film medium which allows for levitation. Recently Atalla et al. [15] have studied the levitation phenomenon found in the incompressible fluid thin film and in the special case that was described, the levitation predominantly stemmed from the convective acceleration of the fluid film. This validation of fluid film levitation in liquid environments meant that in theory friction modulation can be achieved in endoscopes. This recent achievement sparked the concept for this research.

B. The previous design

In this section, the previous concept that was designed and produced by Tuijp et al. [5] is explained and shown in figure 3b. This resonant element features an inner ring, an outer ring, and four radial beams that act as compliant hinges, all of which are cut from a single piece of titanium. The area between the inner and outer rings is divided by radial beams, which create four separate cavities. A piezo is glued in place in the indent on the inner wall of the outer ring. As described by Tuijp, these four piezos allow the desired mode shape to be achieved. In the study, both numerical and experimental studies were conducted on the resonant characterization of the design. The numerical study was performed in COMSOL and a maximum resonant amplitude of 1.74 µm was found at a frequency of 24 400 Hz, the mode shape is shown in figure 3b. The experimental study resulted in both a lower resonant frequency of 19.7 kHz and a smaller maximum resonant amplitude of 1 µm. Besides vibration characterization results, the friction reduction effect is studied. The experiments show that the friction reduction effect can be observed on hard substrates, but is negligible on soft substrates.

The eigenmode shape shows that this design does not approximate free ring vibration. With free ring vibration, the front view of the eigenmode study would be an approximation of an elliptical profile, without the flat plane around the hinges present in this study. The stiffness of the four hinges alters the vibration characteristics. This results in a large discrepancy between the eigenfrequencies of a free-floating outer ring and the entire design with rigidly connected hinges. The desired eigenmode frequency of the outer ring without hinges can be described analytically using

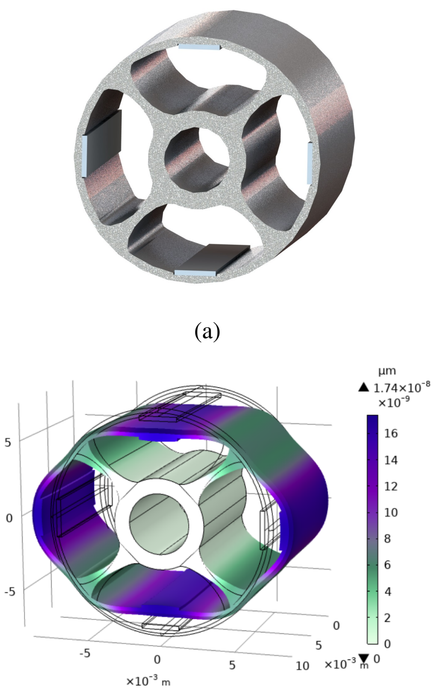

(a)

(b)

Fig. 3: (a) Overview of the previous design. (b) The time-domain study results. A maximum amplitude of $1.74\,\mu\mathrm{m}$ is achieved at $24\,400\,\mathrm{Hz}$ [5]

the equations for free ring vibration, provided by Blevins et al. [16] and results in a frequency of only $9\,\mathrm{kHz}$.

III. DESIGN REQUIREMENTS

To evaluate the performance of the design of the resonant element, multiple design requirements are defined. These requirements are separated into multiple categories. The first category describes global requirements and the second category is based on geometrical design. The geometrical requirements are related to the size and shape of the design.

The first set of requirements is global, so these will be used in all designs. The first requirement is that the outside of the design has to be cylindrical to match existing endoscopes. The second requirement is the use of medical-grade materials. For an endoscope to be used on patients the material from which the endoscope is made has to be safe. This means that the material must not chemically react with the surrounding tissue. This excludes many metals, examples of options that are valid are medical-grade stainless steel and titanium.

Besides these global requirements, there are multiple design-specific requirements. These depend on the size and shape of the design and will therefore vary between the different concepts.

These requirements are as follows

- Resonant frequency: An ultrasonic frequency of over $20\,\mathrm{kHz}$ is desired as the upper limit of human hearing is $20\,\mathrm{kHz}$ [17], and friction-reducing effects can occur around this range [7].
- Resonant amplitude: The friction-reducing squeeze film effect is prevalent in the micrometer range [7].
- Outer diameter: The outer diameter of the endoscope is a determining factor for the applicability of the design. The maximum outer diameter of the endoscope is determined by the vessel in which it is to be used. A colonoscope, which is used in a colonoscopy can have a larger outer diameter than a catheter, which is used in a much smaller blood vessel.
- Internal size: Open internal space in the design is crucial to allow optical or mechanical wires to pass through the design and span from the working end of the endoscope to the handle which the surgeon uses to interact with the working end. Relatively large, uninterrupted open space is desirable as this will in turn increase the applicability of the design.
- Ease of Assembly: A medical device is preferred to be either reusable or disposable. Since these designs require expensive precision engineering, being reusable is desired. Therefore it has to be possible to disassemble the device and clean it to medical standards. The assembly being waterproof is more desirable.
- Adaptability: To facilitate as broad as possible range of surgeries, the adaptability of the design is crucial. This metric describes how much the performance of the design is affected by altering various dimensions.

The design-specific requirements are used to evaluate and compare the designs.

IV. THE NEW DESIGN

A. *The initial design*

The new design, shown in figure 4, strives to be as close as possible to what can be considered free ring vibration. The conceptual idea behind the new design is to minimize the influence of the support structure on the frequency response of the outer ring. The separation of the outer ring from the inner support structure is the first step to achieve this goal, shown in figure 4. Instead of rigidly connected hinges, the new design features sliding contacts. Aside from friction, the sliding contacts should allow unhindered rotation of the outer ring. The support structure will be made out of a material that possesses self-lubricating properties in combination with the titanium of the outer ring, further reducing the influence on free rotation. In the highlighted section in figure 4, the sliding contact surface is located on the midplane of the wall, where there is theoretically no translation. Therefore both the rotational and translational influence should be minimized. The cutouts also align the support contact with the vibration nodes. However, even with these adaptations the design still incorporates piezos mounted on the inside of the outer ring and is thus inherently in-homogeneous and will never exactly match the requirements for free ring vibration. Even with this limitation, the new design has several advantages over the previous design. The first is that the outer ring approximates free ring vibration, and the desired eigenmode can be estimated using the equations from Blevins et al. [16].

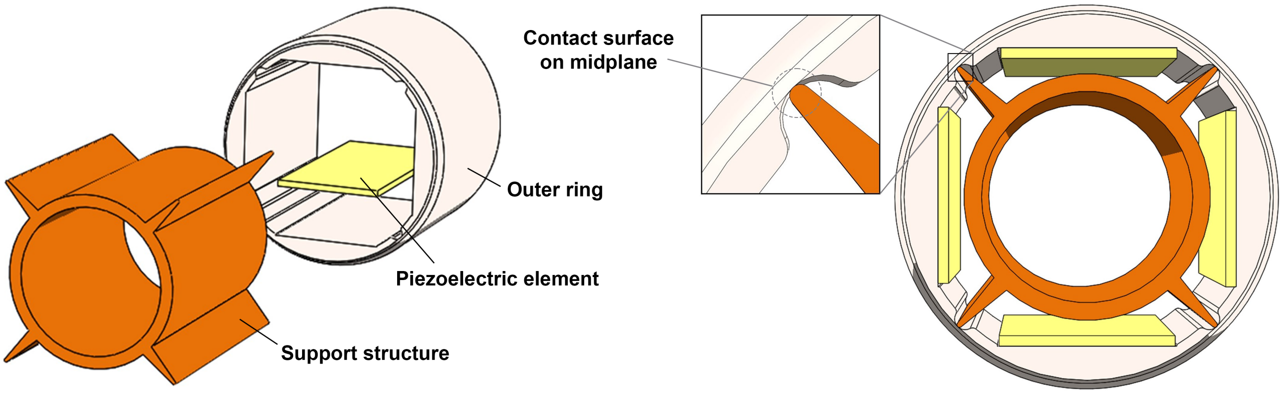

Fig. 4: The overview of the new design. The midplane support contact is highlighted. The ring is shown in white, the piezoelectric elements in yellow and support structure in orange.

The ability to approximate the resonant behavior analytically obviates the need for time-consuming iterative numerical simulations The complexity of adapting existing endoscopes to incorporate friction-modulating elements is also reduced. Since the response is less dependent on the inner structure, the design of the inner structure can be adapted to interface with existing endoscopes. Lastly, without the support structure permanently in place, a larger cavity remains. This makes the assembly process, where the piezos have to be glued in place and wires are soldered, less complex.

The second set of changes is dimensional, the outer diameter is reduced from the previous 15 mm down to 11 mm. This is combined with an increased wall thickness from 0.5 mm to 0.6 mm to increase the resonant frequency above 20 kHz. The width of the piezos is increased from a previous 2.5 mm to 5 mm. Increasing the width of the piezo increases the power input, which can lead to an increase in the resonant amplitude. It also simplifies the production process since the piezos no longer need to be cut lengthwise.

With the assumption that the influence of the inner structure is minimal, the total system response can be approximated using just the outer ring. The outer ring modelled is imported into COMSOL where eigenfrequency and frequency-dependent studies are conducted. The starting point for this study is the eigenmode frequency found in the analytical calculation. The eigenfrequency study finds multiple eigenmodes in a range around this value. From these results, the desired eigenmode is selected. This eigenmode is shown in figure 5a. This eigenfrequency value is carried over to a frequency-domain study, where a range around this value is simulated. This frequency domain study contains the amplitude data shown in figure 5b. Figure 5a shows that the amplitude is not constant along the length of the ring, but slightly higher near the edges. The highest average amplitude along the anti-nodal line of 3.13 µm occurs at an eigenfrequency of 22 752 Hz. The maximum amplitude at this frequency is 3.49 µm.

B. *Later additions*

Preliminary testing indicated the need for several additions to the design. The first addition to the design was the fillet on the outer edges. This addition was made to stop the edge of the ring from catching while sliding along a deformed surface or in case the contact surface is not parallel to the sliding direction. Another addition to the design is the implementation of a 0.3 mm recess along the front and back edges of the ring, which aims to aid in waterproofing. With this recess, the sidecaps are countersunk into the ring. This recess significantly increases the surface area to which glue can adhere, most importantly it creates an overlap that allows a portion of the glue to be loaded under shear stress instead of normal forces.

V. PROTOTYPE PRODUCTION

Production of the prototype starts with the production of the titanium ring at DEMO, a machining facility at TU Delft. Next is the application of the piezoelectric plates on the inner faces of the ring. The piezoelectric plates are cut to a length of 10 mm. A thin layer of epoxy adhesive is applied to one of the inner faces of the ring and the piezo is then put in place and gently pressed down. A wedge system applies even pressure to the surface of the piezos during the curing process. Then copper wires are soldered onto the electrodes on the piezos. Lastly, the support structure and sidecaps are pressed in place. The assembled prototype is shown in figure 6. Appendix VI describes the production process in greater detail.

VI. RESULTS

The experiments aim to study the friction reduction effect under varying circumstances. The influence of the normal load, applied voltage, test substrate material, ring orientation, and test substrate surface channel diameter on the performance of the prototype is studied. Multiple measurements are conducted to better understand the mechanisms that are at play. These mechanisms are studied through combinations of multiple sensors. These include force data from the six-axis force sensor, vibration amplitude using a laser Doppler

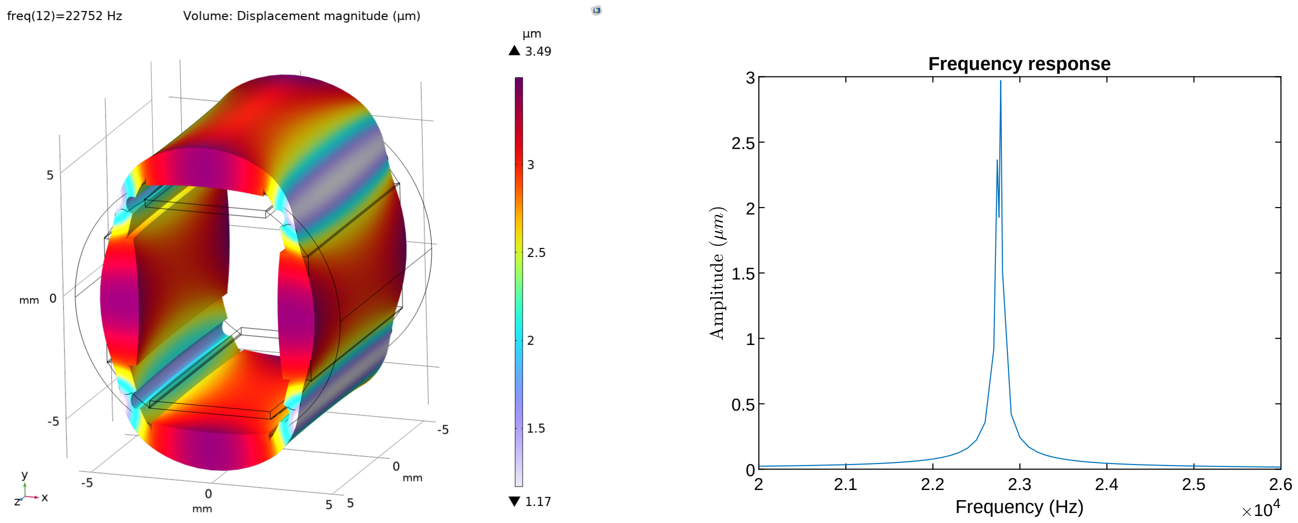

(a)

(b)

Fig. 5: Time-domain study of the new design in COMSOL (a) the eigenmode shape, the desired mode shape is achieved at $22\,752\,\mathrm{Hz}$ with a maximum amplitude of $3.49\,\mu\mathrm{m}$ (b) The average amplitude along the anti-nodal line. An average amplitude of $3.13\,\mu\mathrm{m}$ along the anti-nodal line is achieved at $22\,752\,\mathrm{Hz}$

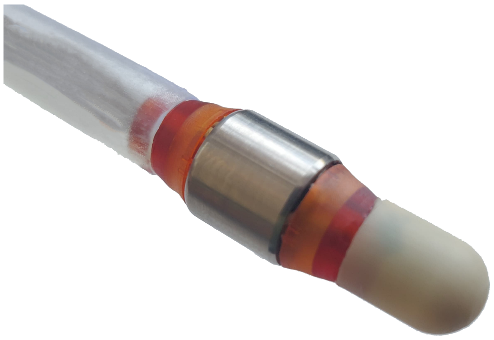

Fig. 6: The assembled prototype at the tip of a mock-up endoscope.

vibrometer, and levitation height using a laser distance sensor.

A. *Laser Doppler vibrometer*

As there might be a discrepancy between the modeled frequency of the desired mode shape and the actual frequency at which this mode shape occurs, a frequency sweep is conducted. The laser Doppler vibrometer (Polytec OFV-5000) is used to measure the maximum velocity normal to the surface of the ring. Since the vibration of the ring is harmonic, this maximum velocity, together with the frequency, can be used to calculate the vibration amplitude. An up-chirp signal is used for the frequency sweep, this is a signal in which the frequency increases with time. By measuring the resonant amplitude throughout this chirp signal, the actual resonant frequency of the ring can be determined. During this measurement, the LDV is aimed at the center of the anti-node as this is where the maximum amplitude is expected. However, as the frequency sweep is conducted with the LDV only measuring a small point in the center of the anti-nodal line, this does not yet confirm that the desired mode shape is achieved.

To confirm that the desired mode shape is achieved, a grid along the entire surface of the ring is scanned. This scan is conducted through the addition of a servo motor (Tower Pro SG90), powered by a standalone 5V power supply and controlled with an Arduino. The LDV scans 11 points along the red line on the top of the ring surface. As depicted by the red plane in figure 7a After these 11 points have been scanned, the servo motor rotates the ring 10°. After 180° of rotation, the ring is manually rotated 180° to scan the other half. The results from this measurement are shown in figure 7b. The amplitude map shows 4 dark blue lines, which represent low-amplitude regions. These four low-amplitude lines outline areas of increasing amplitude. The phase map shows two sets of areas with 90° and −90° phase offset.

B. *Force sensor setup*

An overview of the friction force setup is shown in figure 8a. The force measurements are conducted using a six-axis force sensor (Nano43 by ATI). Two motorized linear stages (NRT150 by Thorlabs) are used to control the horizontal movement of the test substrate and the applied normal load of the prototype. The vertical stage is connected to the prototype through two clear flexible tubes, whose deflection permits a controlled vertical load application while allowing some transversal misalignment. Many elements of the setup are printed on a Formlabs 3B printer. The test substrates are printed in model and Elastic 50A resin, the flexible tubes are printed in clear resin and the supporting brackets in model

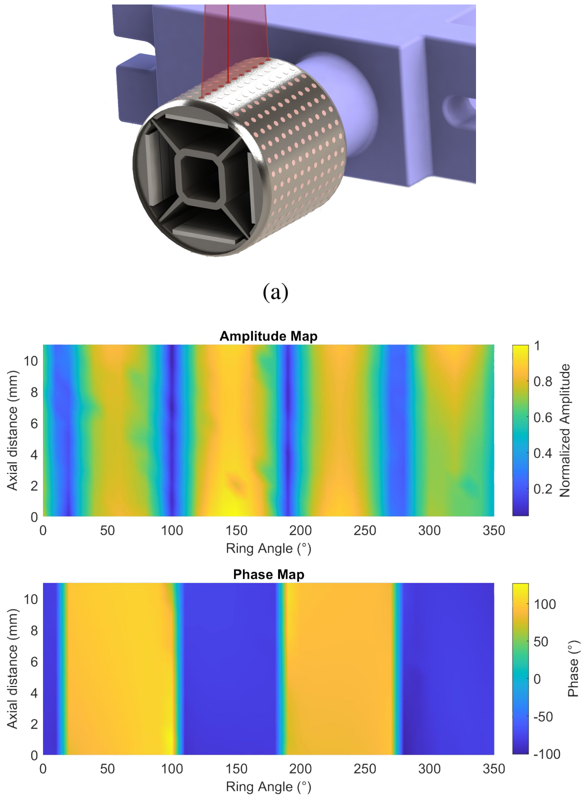

(a)

(b)

Fig. 7: (a) Red dots represent discrete LDV measurement points. (b) Measured mode shape

resin. A close-up of the ring prototype, supported by the side caps and flexible tubes is shown in figure 8b.

The LDV and friction force sensor gather data conjointly in all measurements apart from the levitation height measurements and are used to study the relation between the vibration amplitude and the friction reduction factor in different conditions. To maintain the readability of this report, not all results are noted in this section, specific plots are selected and the rest is in appendix I.

During the friction measurements. the ring is slid along the surface of the test substrate as depicted in figure 8a by the dashed grey line. During a friction force measurement run the first step is setting the desired load using the vertical linear stage. After a settling period, the test substrate is moved $2.5\,\mathrm{mm}$ forwards at a speed of $0.1\,\mathrm{mm/s}$. The acceleration is limited to $0.1\,\mathrm{mm/s^2}$. Five seconds after the movement begins, the vibration is applied for five seconds. Measurements without vibration are referred to as the vibration is 'Off' and in the graphs depicted in red. Measurements with vibration as vibration turned 'On', and is depicted in blue. In the 'On' scenario a levitation layer forms as shown in figure 8c.

The first set of experiments tests the friction reduction effects on hard substrates, at 280 Vpp and 22 552 Hz. In these experiments, the surface of the ring contacts the test substrate on an anti-nodal line. These experiments are conducted for three different channel diameters: $11.2\,\mathrm{mm}$, $18\,\mathrm{mm}$ and $30\,\mathrm{mm}$, or curvature ratio of 0.37, 0.61 and 0.98 respectively in both in air and submerged $3\,\mathrm{mm}$ in water. The results are shown in figure 9a and 9b respectively.

The Friction reduction factor is also measured on a soft substrate with an $18\,\mathrm{mm}$ channel diameter, at 1 N normal load and 280 Vpp. These results are shown in figure 10, and a more detailed result in appendix I-B.

Another test is conducted to study the friction reduction factor along the rest of the ring surface. For these tests, the ring is rotated $22.5°$ from the anti-nodal line, and also to the nodal line as shown in figure 12a. These tests are conducted with an applied voltage of 280 Vpp, and the $18\,\mathrm{mm}$ channel diameter substrate. The results are shown in figure 12b.

The friction reduction as a function of the voltage amplitude is tested by varying the peak-to-peak input voltage linearly between 40 and 280 volts over a period of 5 seconds. This test is conducted on a hard $18\,\mathrm{mm}$ channel diameter substrate in both air and water conditions. The results are shown in figure 13a and 13b.

C. Levitation height

The levitation height is obtained using a laser displacement sensor (LDS), the specific model is the Keyence LC-2420. The laser distance sensor measures the vertical distance between the sensor and the surface of the ring. The distance change between with and without vibration is the levitation height. An example of this result is shown in figure 14, and others are found in appendix I-C.

VII. DISCUSSION

A. Vibration characteristics

The vibrational characteristics of the ring as modeled in COMSOL resulted in a resonant frequency in the desired mode shape of $22\,752\,\mathrm{Hz}$ and an average amplitude along the anti-nodal line of $3.13\,\mu\mathrm{m}$. These values are expected to differ slightly from the experimental values for multiple reasons. The first is a result of simplifications of the model. Such as the omittance of the epoxy adhesive layer between the ring and piezo. This layer is expected to be very thin and should have a negligible effect on the performance of the ring. The same applies to the wires that power the piezos, this is discussed further in Appendix II. Another reason is inaccuracies in the assembly process. Even though the titanium ring and untrimmed piezos are produced with strict tolerances, trimming the piezos to size and controlling the placement when the wedge system is inserted remains inaccurate. With these limitations, the resonant properties varied per produced prototype. However, the resonant frequency was generally within $100\,\mathrm{Hz}$ of $22.5\,\mathrm{kHz}$ and the amplitude as per figure 13a and appendix I, around $3\,\mu\mathrm{m}$. These results are very close to the modeled results. The mode shape measurements resulted in the amplitude map shown in figure 7b. This shows 4 low-amplitude lines, which are nodal lines. In between these nodal lines, there are 4 anti-nodes. The fact that these areas are axially constant and adjacent areas have a $180°$ phase shift, confirms that the desired mode shape is achieved.

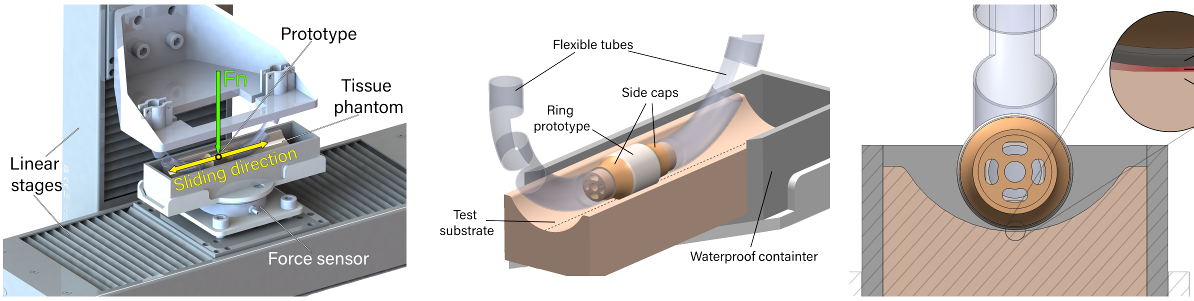

(a) (b) (c)

Fig. 8: (a) An overview of the setup. The sliding direction (yellow) and the applied normal force (green) that are used in the friction force experiments are shown (b) A close-up of the assembly that holds the ring in place (c) A schematic representation of the levitation layer. High pressure is denoted as red, which decreases to ambient pressure towards the edges

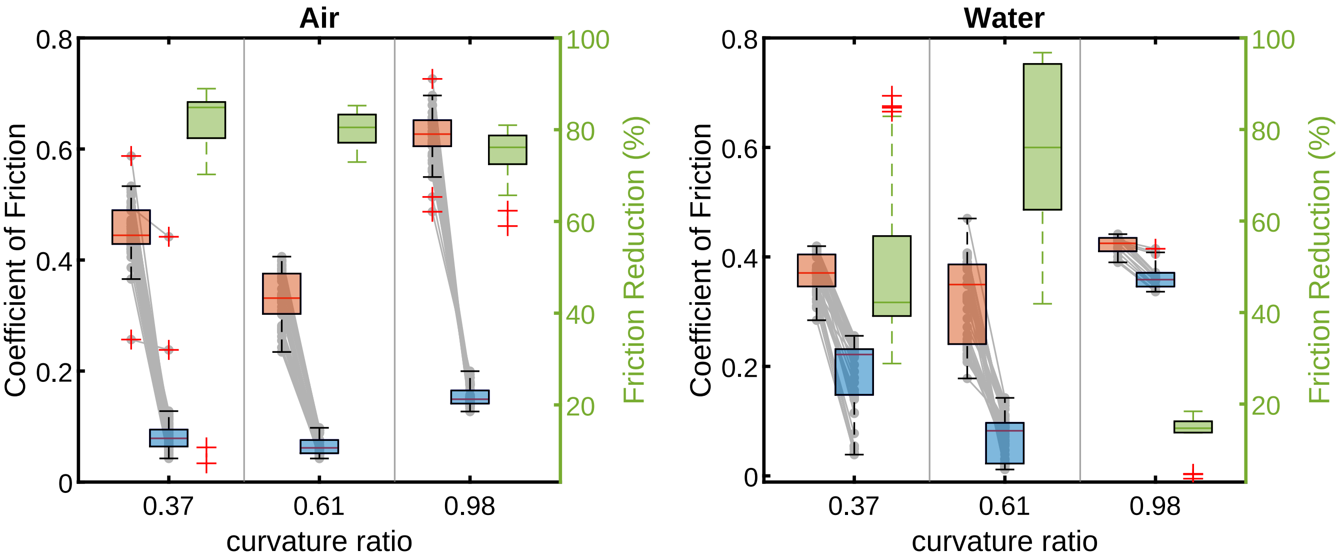

(a) (b)

Fig. 9: Force measurement results on hard substrates (a) in air (b) in 3 mm water layer. Vibration off in red, vibration on in blue, and friction reduction in green.

Appendix II shows possible issues that have been uncovered and resolved during testing.

B. Friction reduction factor

The tactile results, or friction reduction testing based solely on touch are very significant. This is not a quantified result, but it was noticeable even to persons without prior experience in haptic interactions. As is briefly described in section II-A, and based on the equations stated by Shi et al. [6] for air and Atalla et al. [15] for incompressible liquids, the friction reduction factor is dependent on multiple variables, such as vibration amplitude and frequency, contact area, fluid density, and normal load. The fact that this design is circular, and thus the contact surfaces are not parallel. Therefore, the substrate curvature ratio is added to the list of variables. These variables, apart from the resonant frequency which is determined by the resonant frequency of the ring, are studied in multiple experiments. The following section describes the results of these experiments.

Figure 9a shows that although the on and off friction coefficients do vary between the different curvature ratios, the reduction percentage is around 80%. Figure 15 in appendix I-A includes a more detailed overview and shows that the friction reduction increase is limited between 2 µm to 3.5 µm, but this will be studied in more detail later.

Figure 9b and figure 16 in appendix I-A shows a more complex result. The 18 mm substrate performs the best out of the three, with between 60% and 90% friction reduction depending on the load, at vibration amplitudes between 1 µm to 1.2 µm. This is followed by the 30 mm substrate, which achieves between 35% and 90%, at vibration amplitudes between 0.7 µm to 0.9 µm. The 11.2 mm substrate achieves below 20% reduction on average, at vibration amplitudes around 0.2 µm. It is thought that this low amplitude is the result of entrapment of the ring, where the high curvature ratio results in a very high damping effect on the ring.

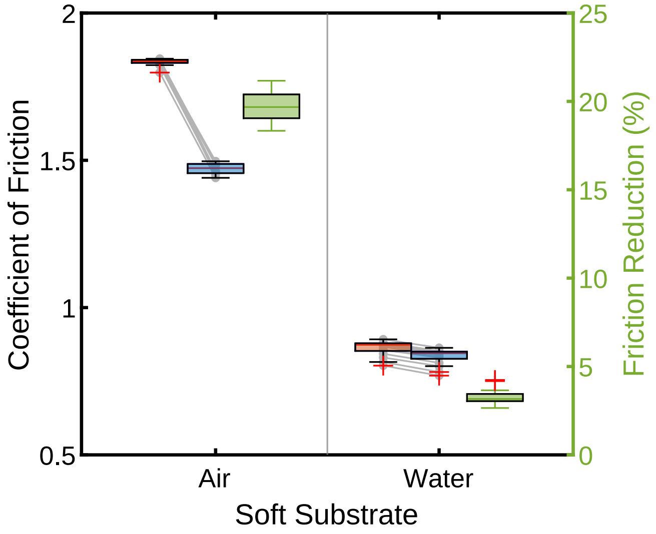

Fig. 10: Force measurement results on 18 mm Elastic 50A substrate. Vibration off in red, vibration on in blue, and friction reduction in green.

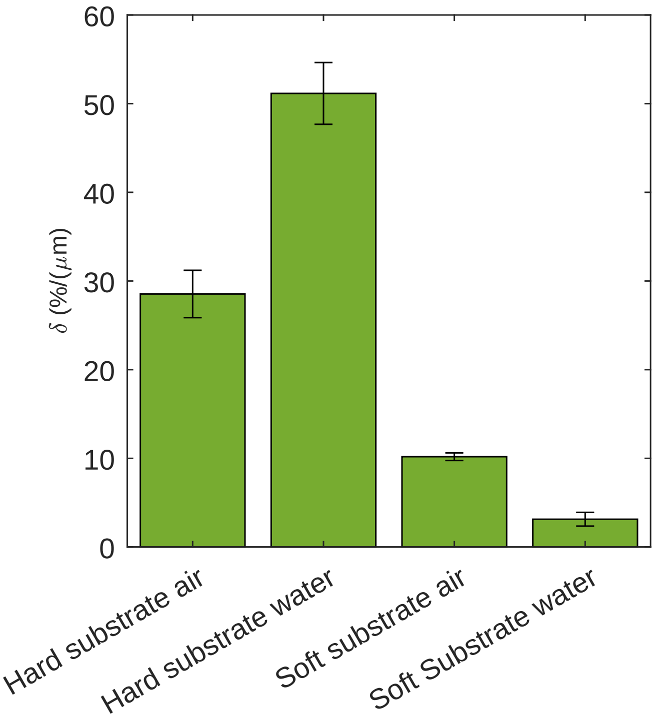

Fig. 11: The friction reduction percentage per micrometer of vibration amplitude, shown as δ in the graph, for hard and soft substrates, in air and in water. The 18 mm substrates are used at 280 Vpp and 1 N normal load.

It might be possible to achieve higher friction reduction percentages at higher vibration amplitude. However, as can be seen in figure 13b, the 18 mm substrate outperforms the 11.2 mm substrate by a large margin at 0.2 µm as well. This suggests that the formation of a levitation layer in very high curvature ratios is limited through another mechanism.

The results from the soft substrate testing show multiple interesting things. The first thing is shown in figure 18a, where 20% friction reduction is achieved at a vibration amplitude of 1.7 µm, whilst with the same vibration amplitude and normal load, over 80% friction reduction is achieved on the hard substrate with the same curvature. The second thing is in the comparison of the results between the in-water input voltage tests (figure 13b) and the in-water soft substrate test (figure 18b). Where a maximum of 0.3 µm vibration amplitude is achieved on the hard substrate, a 0.85 µm vibration amplitude is achieved on the soft substrate. Even with nearly triple the vibration amplitude achieved in the hard substrate, only 5% friction reduction is achieved on the soft substrate. This is especially notable as the 0.3 µm vibration in-water on the hard substrate achieves over 40% friction reduction. These results can indicate that the elastic material of which the soft substrates are made does not feature enough damping to create the phase shift required for higher friction reduction factors. It appears that instead of a levitation layer forming, the soft substrate vibrates along with the ring surface.

Regrettably, the damping constant of the material used (Elastic 50A by Formlabs) in these tests is not specified by the supplier. The description mentions that the material is suitable for part prototyping in situations where silicone would typically be used.

The friction reduction percentage achieved per micrometer of vibration is denoted as δ, and shown in figure 11 for hard and soft substrates, in air and water.

Figures 13a and 13b show the vibration amplitude and friction reduction factor as a function of the input voltage for air and water respectively. Figure 13a displays this relation for four normal loads. A higher normal load is expected to increase the film pressure and thus the damping on the vibration, therefore it is logical that the vibration amplitude rises more quickly in lower normal load measurements. This is seen in the vibration amplitude figure as an approximately proportional difference along the input range between the 0.25 N and 1 N results. As the levitation force created by the vibration amplitude effectively reduces the contact force, a higher friction reduction factor is found for lower normal forces at lower input voltages. This can be very clearly observed around 60 V, where the friction reduction factor increases rapidly for lower loads, and slower with increasing load.

As the input voltage continues to increase, a point arises where the friction reduction factor begins to decrease again, and the distance between the maxima for each normal load appears constant. This can be caused by a number of effects. The first possibility is that other, higher-order, vibration modes might be excited. These higher-order modes

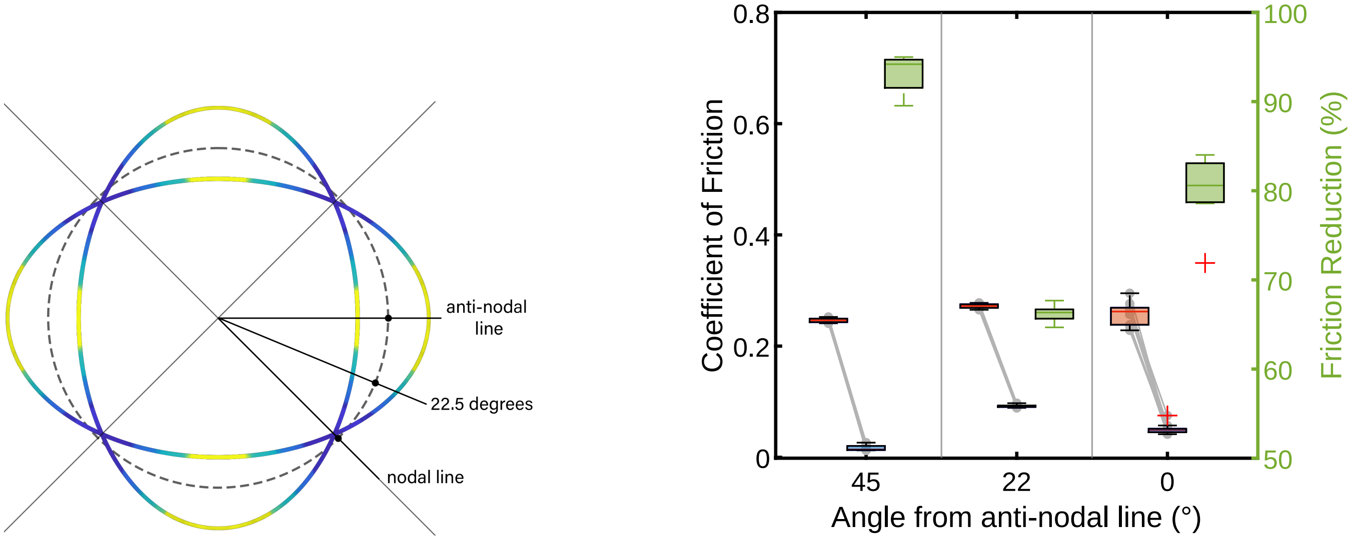

(a)

(b)

Fig. 12: (a) The three orientations (b) The results. Vibration off in red, vibration on in blue, and friction reduction in green.

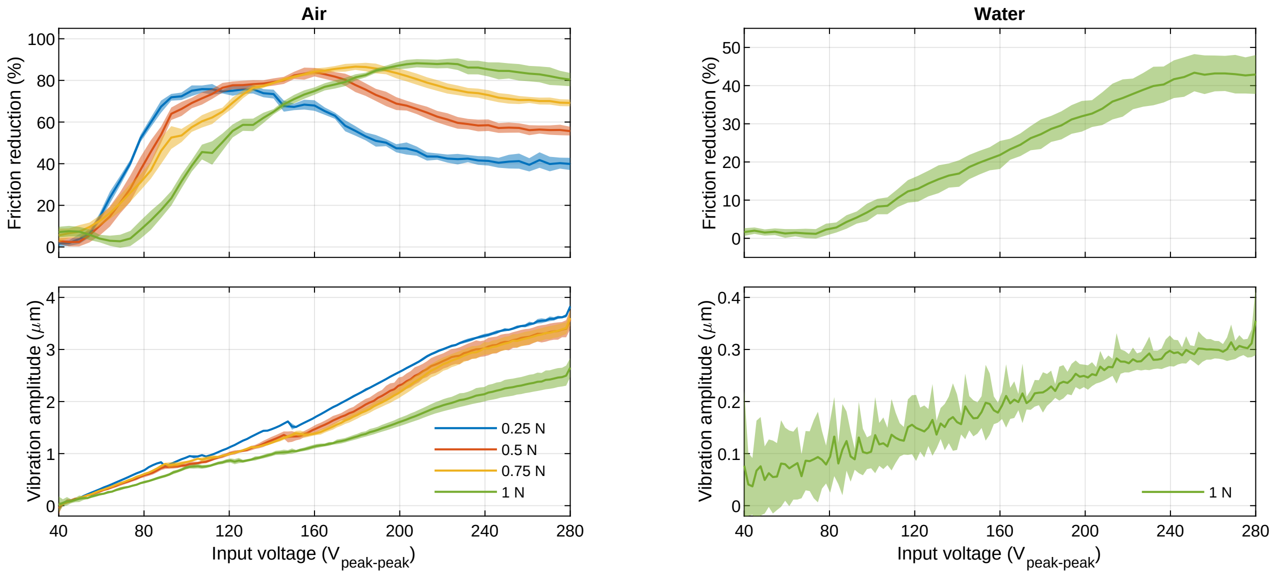

(a)

(b)

Fig. 13: Friction reduction and vibration amplitude as a function of voltage input at 1N normal force (a) in air (b) in water

can feature lower friction modulation at the same vibration amplitude. The same effect can be found in the case of an increase in temperature over time. The next eigenmode found in the COMSOL eigenmode study occurs at around 1 kHz above the frequency of the desired mode. Another possibility is that the ring is intermittently contacting the substrate around the maximum amplitude. A way to effectively study this behavior is to measure the levitation height and vibration amplitude simultaneously. Another possibility might be that it is the result of the dynamics of the entire system, or imperfections of the substrate, both of which can be tested through reversal of the test parameters.

As water is far denser than air, it is expected that the vibration amplitude in water at the same voltage will be smaller, which is confirmed by figure 13b. However, the friction reduction at 0.3 μm amplitude in water is larger than the same amplitude in air. This is clearly shown in figure 11. Atalla et al. [15] compared the amplification factor, which is the ratio between levitation height and vibration amplitude for incompressible and compressible fluids. They found that at the same mass, a significantly greater amplification is found in water than levitation in air, and thus the 0.3 μm

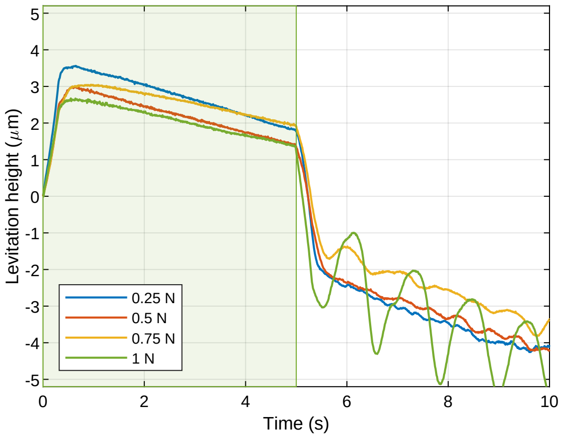

Fig. 14: Levitation height for different normal loads.

amplitude in water yields a larger levitation height.

The levitation height measurement results are shown in figure 14 and in appendix I-C. Figure 14 shows different levitation heights for different normal loads. As expected a higher normal load results in a lower levitation height.

A static drift in the levitation height of around 0.5 µm per second can be seen throughout the entire measurement set. This can be caused by the substrate not being exactly level. Besides the drift, a slight up-and-down movement of the ring can be observed outside of the shaded green region, this can be due to the ring pitching down as a result of an increased friction coefficient, which can lead to the front of the ring digging into the substrate. As the sensor is aimed at the center of the ring, this pitching can result in up-and-down movement. With the increased friction coefficient, stick-slip can occur and thus result in periodic pitching. This hypothesis is supported by the fact that these oscillations increase in amplitude as the normal load increases.

The results from the 11.2 mm and 30 mm substrates are not consistent with the results from the 18 mm substrate. It is thought that these results are affected by misalignment between the center of the ring and the center of the substrate curvature. This causes the ring to move across the substrate perpendicular to the sliding direction, which results in an incorrect measurement. As the ring is cylindrical, this perpendicular movement causes the focal point of the laser to move down or even up along the circumference if the focal point is improperly aligned. However, unlike the static drift experienced in the 18 mm substrate, these deviations can not be corrected. The measurement can be improved in two ways; by using a second LDS to measure the horizontal movement perpendicular to the sliding direction, or by conducting the same measurement without sliding.

The friction reduction effect is expected to be maximal in the anti-nodal line, and minimal at the nodal line. For this reason, the effect of the orientation is studied. These results are shown in figure 12b. These results show that the friction reduction is decreased at 22.5°. At the nodal or 45° line, however, the friction reduction factor is far greater than expected. This can in part be explained by the fact that the contact surface is spread out along the circumference of the ring and therefore the contact patch is not limited to only the nodal line. Another part of the friction reduction is thought to be the result of vibrations tangential to the surface. These tangential vibrations are present in the simulations but have not been measured in the prototype. Lastly, and most likely the largest contributor is that the reliability of the 22.5° and 45° degree measurements is limited. The setup used for these measurements was required to allow the rotation of the ring relative to the substrate and was less rigid as a result. This resulted in stick-slip in many measurements.

C. *Limitations*

Multiple prototypes have been constructed and used in testing over the span of this research. As is described in appendix III, various elements of the ring can fail and require replacement. Thus the various tests were not all conducted using the same prototype. Individual tests were conducted with the same prototype, but there may be some discrepancies in performance between test types.

D. *Future research*

The friction reduction behavior near the nodal lines is not yet fully understood. The vibration amplitude in the normal direction on the nodal lines should theoretically be zero. Without normal vibration, no squeeze film should develop and thus no friction modulation should be present. However, it was shown that a significant friction reduction is still achieved on the nodal lines. One explanation is that the contact patch is not strictly limited to the nodal line itself, but instead spans an area around the nodal line, and that a squeeze film can develop near the outer edges of the contact patch. Tangential vibrations should theoretically also be zero, but the presence of these vibrations could also explain the friction reduction. The inclusion of levitation height measurements could also clarify some of this behavior. Further insight into the mechanisms at play can also be gained by conducting a similar study to those conducted by Friesen et al. in 2017. They studied the contribution of the squeeze film layer to the friction reduction factor by conducting friction experiments at both atmospheric pressure and in a vacuum. This study showed that the squeeze film layer was responsible for 98% of the friction reduction [7]. A similar study could be conducted to study the squeeze film's contribution to friction reduction.

Combining measurements from the LDV with improved LDS data can shed great insight into the mechanisms around both compressible and incompressible fluid film levitation. The combination of both measurements would be beneficial in the discussions on curvature ratios in both air and water, the levitation height, input voltage modulation, ring orientation, and soft substrate performance. The current friction force measurement setup allows either the LDV or LDS to be used, but these two can not be used simultaneously since the two sensors would interfere. A solution would be to roll the entire friction setup 90° and aim the LDV at the side of the ring.

Currently each piezo is powered and ground by one wire, resulting in eight total wires per element. An option would be to ground all piezos using a single wire and another for each opposing pair. These three wires can then be daisy-chained together with the other rings along the length of the endoscope to maximize the remaining lumen space.

Lastly, the next version of the design is described in appendix V. The validation of the performance of the miniaturized version is the next big step in the proof of concept.

VIII. CONCLUSION

The goal of this paper was to improve on the previous design of a friction-modulating ultrasonically vibrated ring. This paper evaluates the previous concept and builds upon it. The design and production processes are described and experimental testing is conducted. The developed finite element model of the vibration characteristics is proven to accurately simulate the physical prototype. Using the developed test setup, the performance of the ring on hard and soft substrates in both compressible and incompressible fluids is quantified. Friction testing shows that up to 90% friction reduction can be achieved on hard substrates in both air and water. On the soft substrate used in testing, up to 20% reduction can be achieved in air and 4% in water.

The conjunction of data gathered from multiple sensors simultaneously reveals the relationships between the test substrate curvature, normal load, ring orientation, vibration amplitude; and the friction reduction factor. Some insight is gained into the fact that the in-water performance is dependent on the curvature ratio between the vessel and the ring. The results also show that the voltage input required to achieve the maximum friction reduction is dependent on the applied load and fluid density.

Experimental testing of the prototype confirms that the concept can achieve fluid film levitation in both compressible and incompressible fluid environments and thereby validates the proof of concept.

ACKNOWLEDGEMENTS

I would first like to thank Mostafa A. Atalla (TU Delft) for providing daily supervision. Further, I would like to thank Zhaochong Cai (TU Delft) for providing input and advice, and Jeroen Tuijp for discussing the previous concept. Lastly, I would like to thank Maurits Pfaff (TU Delft) and Remi van Starkenburg (DEMO) for their contribution to the production of the prototypes.

REFERENCES

[1] R. A. Lange and L. D. Hillis, "Diagnostic cardiac catheterization," *Circulation*, vol. 107, 5 2003. [Online]. Available: https://www.ahajournals.org/doi/10.1161/01.CIR.0000070982.94049.A2

[2] S. Nagaoka and R. Akashi, "Low-friction hydrophilic surface for rne c devices."

[3] K. Ikeuchi, T. Takii, H. Norikane, N. Tomita, T. Ohsumi, Y. Uyama, and Y. Ikada, "Water lubrication of polyurethane for medical use grafted with dimethylac lamide," pp. 179–185, 1993.

[4] A. Ali, D. Dodou, G. Smit, R. Rink, and P. Breedveld, "Stabilizing interventional instruments in the cardiovascular system: A classification of mechanisms," *Medical Engineering & Physics*, vol. 89, pp. 22–32, 2021. [Online]. Available: https://www.sciencedirect.com/science/article/pii/S1350453321000084

[5] J. Tuijp, "Friction modulation in endoscopes: A proof of concept."

[6] M. Shi, K. Feng, J. Hu, J. Zhu, and H. Cui, "Near-field acoustic levitation and applications to bearings: A critical review," *International Journal of Extreme Manufacturing*, vol. 1, no. 3, 2019.

[7] R. F. Friesen, M. Wiertlewski, M. A. Peshkin, and J. E. Colgate, "The contribution of air to ultrasonic friction reduction." Institute of Electrical and Electronics Engineers Inc., 2017, pp. 517–522, cited By 3. [Online]. Available: https://www.scopus.com/inward/record.uri?eid=2-s2.0-85034213617&doi=10.1109%2FWHC.2017.7989955&partnerID=40&md5=5314af3497e8432688131a2eee18caaf

[8] Y. Abe, M. Fujiwara, Y. Makino, and H. Shinoda, "Remote friction reduction on resonant film surface by airborne ultrasound," *IEEE Transactions on Haptics*, vol. 14, no. 2, pp. 260–265, 2021. [Online]. Available: https://www.scopus.com/inward/record.uri?eid=2-s2.0-85105076368&doi=10.1109%2FTOH.2021.3075979&partnerID=40&md5=23b38e1a04556d7f27c6f6e7da08c4c4

[9] S. Ghenna, C. Giraud-Audine, F. Giraud, M. Amberg, and B. Lemaire-Semail, "Control and evaluation of a 2-D multimodal controlled-friction display," in *2017 IEEE World Haptics Conference, WHC 2017*. Institute of Electrical and Electronics Engineers Inc., 2017, pp. 593–598. [Online]. Available: https://www.scopus.com/inward/record.uri?eid=2-s2.0-85034233282&doi=10.1109%2FWHC.2017.7989968&partnerID=40&md5=2686884228922c0bc4da7204fb9893b5

[10] N. Huloux, L. Willemet, and M. Wiertlewski, "How to measure the area of real contact of skin on glass," *IEEE Transactions on Haptics*, vol. 14, no. 2, pp. 235–241, 2021. [Online]. Available: https://www.scopus.com/inward/record.uri?eid=2-s2.0-85105041928&doi=10.1109%2FTOH.2021.3073747&partnerID=40&md5=3237dfff0f1abde9e18fafdd57fdc4de

[11] T. Ohmori, Y. Abe, Y. Someya, M. Fujiwara, Y. Makino, and H. Shinoda, "Refriction: Remote friction control on polystyrene foam by ultrasound phased array," in *SIGGRAPH Asia 2019 Emerging Technologies, SA 2019*. Association for Computing Machinery, Inc, 2019, pp. 40–41. [Online]. Available: https://www.scopus.com/inward/record.uri?eid=2-s2.0-85076671911&doi=10.1145%2F3355049.3360522&partnerID=40&md5=37f09866ab082f5afa196e4b27adefaf

[12] S. Pan, D. Wang, and W. Huang, "A novel small motor measurement system based on ultrasonic bearings," *Measurement: Journal of the International Measurement Confederation*, vol. 168, 2021. [Online]. Available: https://www.scopus.com/inward/record.uri?eid=2-s2.0-85089413199&doi=10.1016%2Fj.measurement.2020.108307&partnerID=40&md5=115b088cea3e02d80ea0c7dd3a04c95b

[13] K. J. Son, "A nonlinear rheological model for the ultrasonically induced squeeze film effect in variable friction haptic displays," *Korea Australia Rheology Journal*, vol. 29, no. 3, pp. 219–228, 2017. [Online]. Available: https://www.scopus.com/inward/record.uri?eid=2-s2.0-85028951059&doi=10.1007%2Fs13367-017-0023-1&partnerID=40&md5=9e100a3116cc63c7eacdb29d12ea2c95

[14] S. Wang, X. Lu, and H. Sun, "Design and Optimization of Squeeze Film Effect based Tactile Display System," in *2019 IEEE World Haptics Conference, WHC 2019*. Institute of Electrical and Electronics Engineers Inc., 2019, pp. 169–174. [Online]. Available: https://www.scopus.com/inward/record.uri?eid=2-s2.0-85072781809&doi=10.1109%2FWHC.2019.8816147&partnerID=40&md5=3c5800d9f91685bda1f1b344157523ab

[15] M. A. Atalla, R. A. J. van Ostayen, A. A. Sakes, and M. Wiertlewski, "Incompressible squeeze-film levitation," 11 2022. [Online]. Available: http://arxiv.org/abs/2211.04579

[16] R. D. Blevins, *12*. R.E. Krieger, 1995, p. 291–321.

[17] S. Rosen and P. Howell, *Signals and systems for speech and hearing*. Emerald, 2010.

[18] F. Giraud, T. Hara, C. Giraud-Audine, M. Amberg, B. Lemaire-Semail, and M. Takasaki, "Evaluation of a friction reduction based haptic surface at high frequency," G. G. J. V. Y. K. K.J., Ed., vol. 2018-March. IEEE Computer Society, 2018, pp. 210–215, cited By 8. [Online]. Available: https://www.scopus.com/inward/record.uri?eid=2-s2.0-85047940964&doi=10.1109%2FHAPTICS.2018.8357178&partnerID=40&md5=6c5faa9f8d91c73e73c9d07167c8df08

APPENDIX I
MEASUREMENT RESULTS

A. *Substrate channel curvatures*

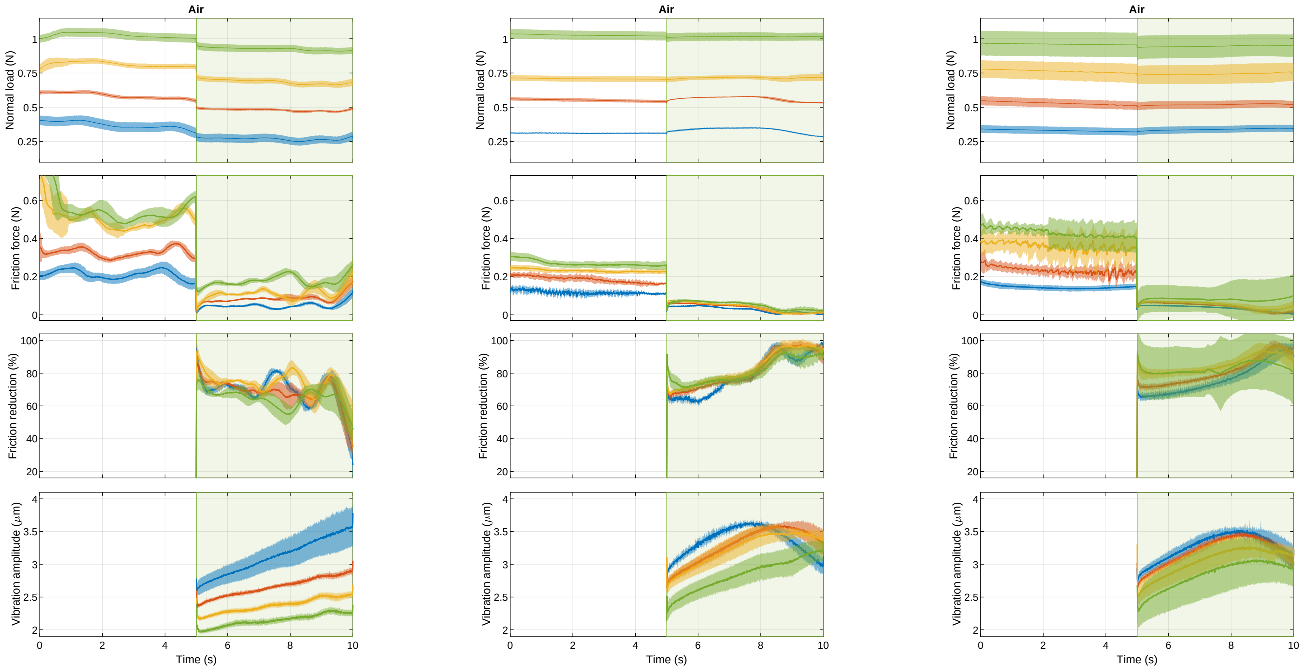

(a) 11 mm hard dry

(b) 18 mm hard dry

(c) 30 mm hard dry

Fig. 15: Hard dry substrates tested at 0.25-1N loads at 280 Vpp. Vibration is on in the green shaded region.

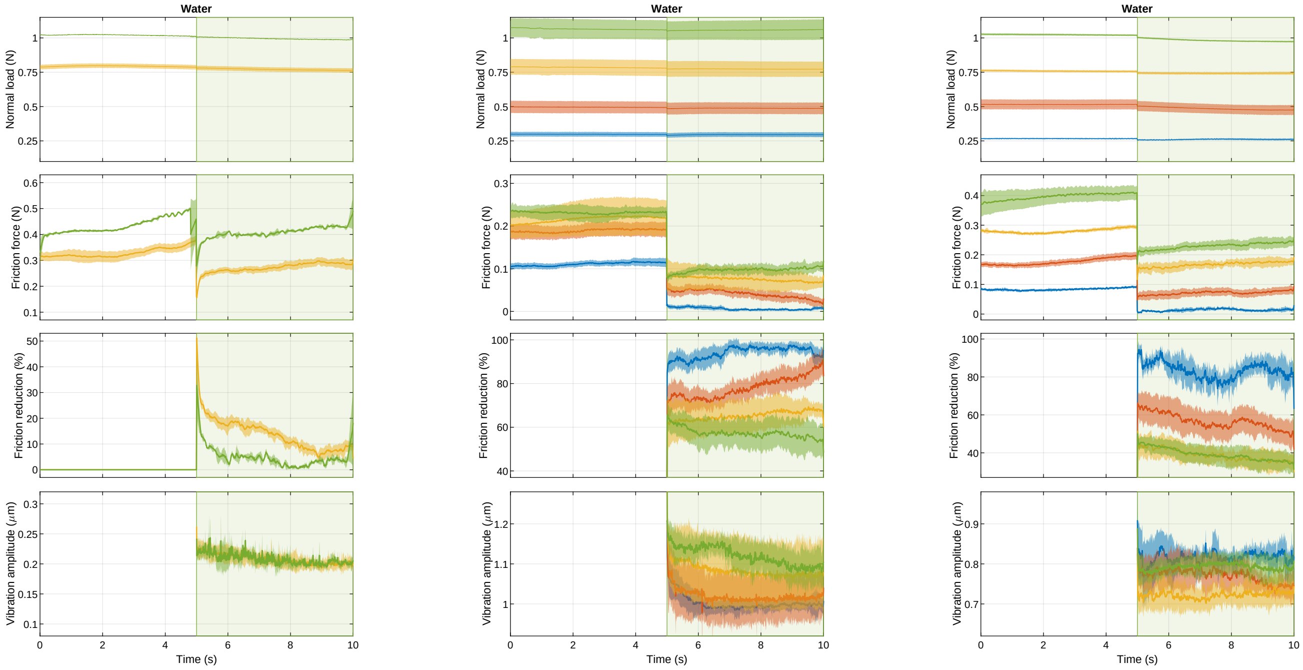

(a) 11 mm hard wet

(b) 18 mm hard wet

(c) 30 mm hard wet

Fig. 16: Hard wet substrates tested at 0.25-1N loads at 280 Vpp. Vibration is on in the green shaded region.

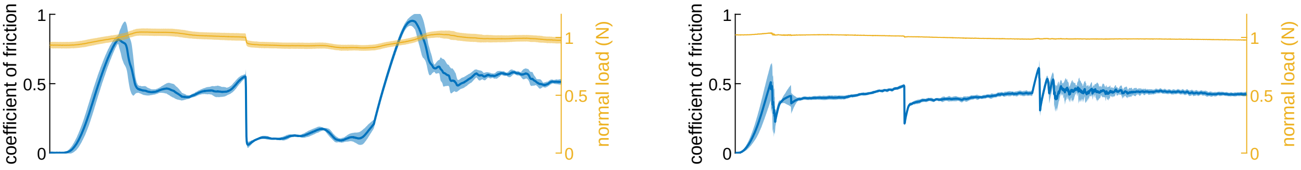

(a)

(b)

Fig. 17: Hard substrate measurements over time in (a) air (b) water.

B. Soft substrate

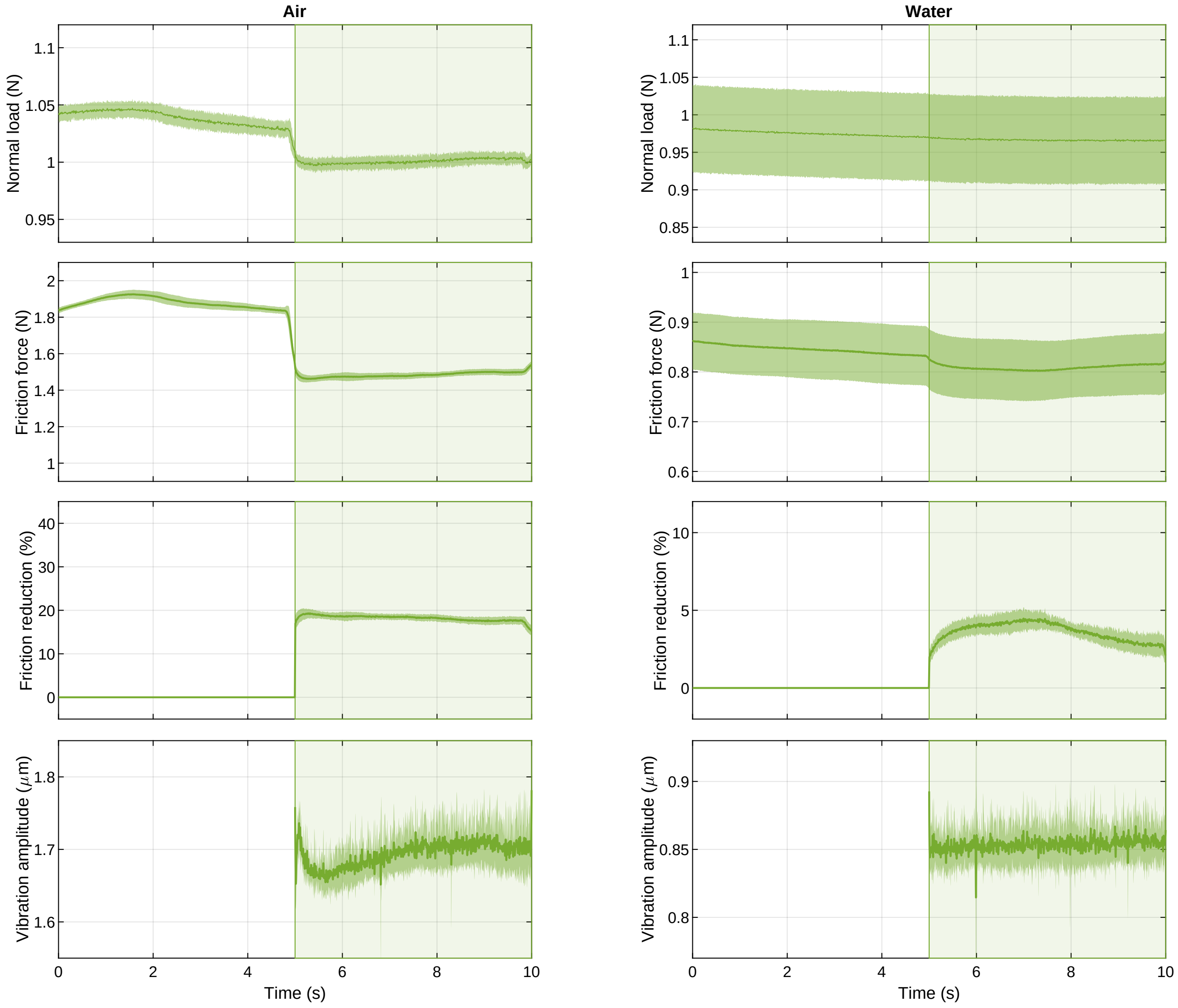

(a)

(b)

Fig. 18: Soft 18 mm substrate tested at 1N normal force at 280 Vpp in (a) air (b) water. Vibration is on in the green shaded region.

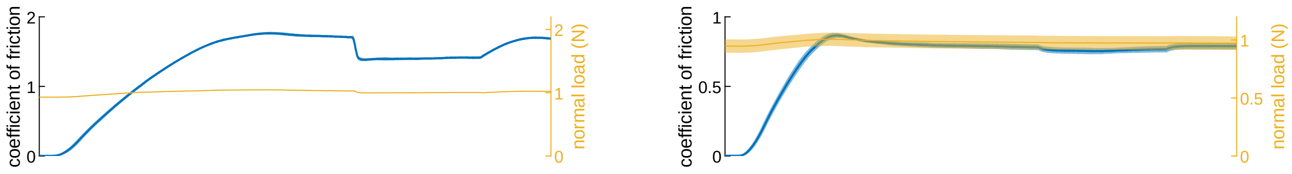

(a)

(b)

Fig. 19: Soft substrate measurements over time in (a) air (b) water.

C. Levitation

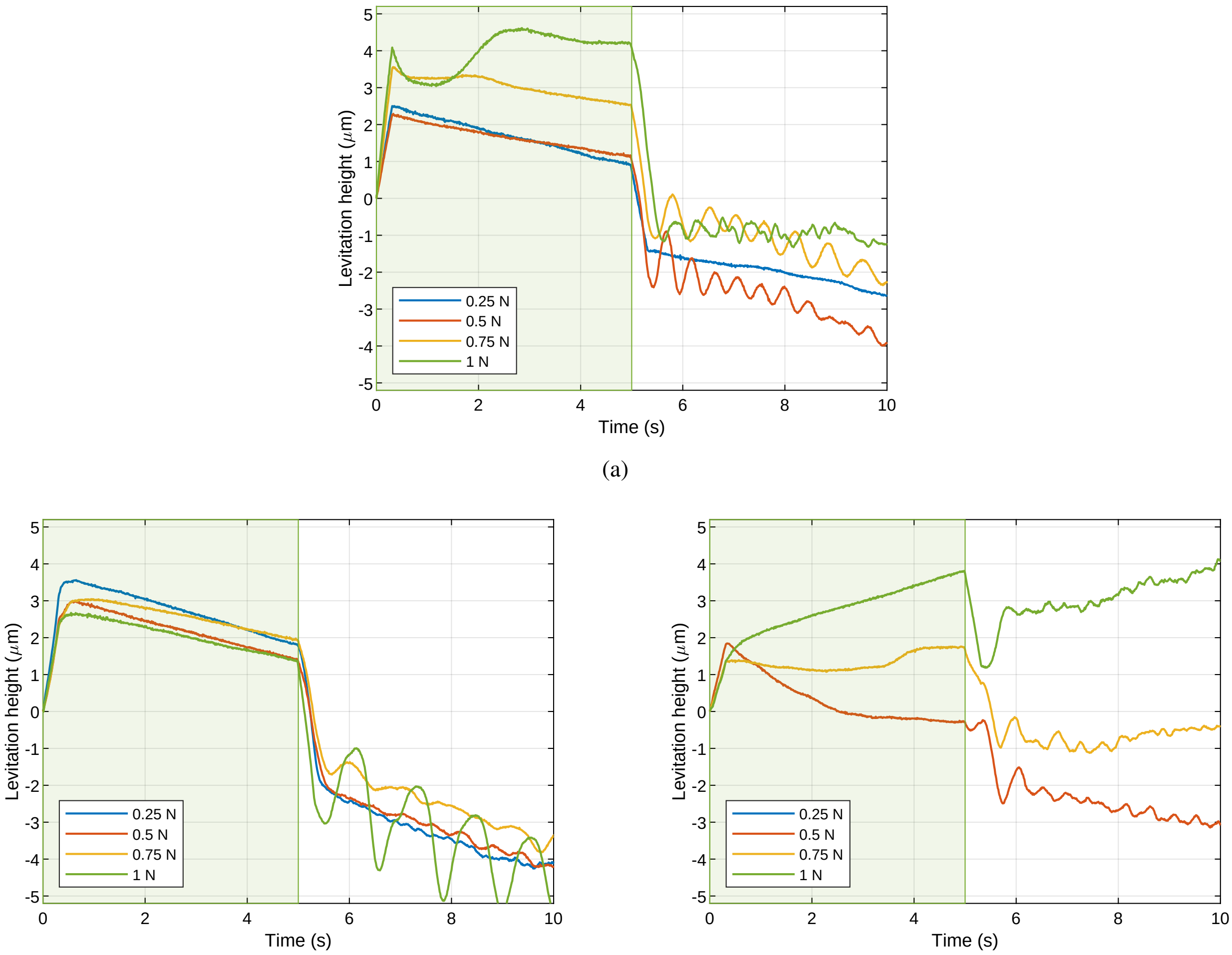

(a)

(b)

(c)

Fig. 20: Levitation height for different normal loads as a function of time. Vibration is applied in the shaded green region, at $t = 0s$ the vibration is activated and a levitation layer is formed. Shown for three substrates (a) 11 mm (b) 18 mm (c) 30mm

APPENDIX II
SOLDERING PATTERN

In the initial prototype, all wires that power the piezos were soldered towards one side, as shown in figure 21a. The idea was that this would make eventual implementation in the endoscope as easy as possible. It was also theorized that a more centered position of additional mass from the wire and solder would yield higher and a more evenly spread vibration mode. This placement did however have its drawbacks. It made the soldering process difficult as the wire located closer to the center of the piezo required the soldering tip to reach far into the ring, which is difficult for the builder. The depth also involves more risk of damage to the surrounding piezos due to increased heat exposure.

(a)

(b)

Fig. 21: (a) wires soldered on one side (b) wires soldered on either side

After measuring the mode shape as described in section VI, the mode shape shown in figure 22a resulted. The amplitude map shows four nodal lines in dark blue which surround four areas. The phase for these areas is as expected, but the amplitude map is not as expected. The results should be nearly constant along the axial length, as shown in figure 5a. Instead of this, a large variation is found in this configuration. On the side where the wires are soldered, the vibration amplitude is far smaller than the side without.

In order to counteract this, the wire that was previously soldered nearest the center of the piezo was moved towards the far end, as shown in figure 21b. The mode shape found for this configuration is shown in figure 22b. This change also made the soldering process easier and reduced the heat exposure to the piezos.

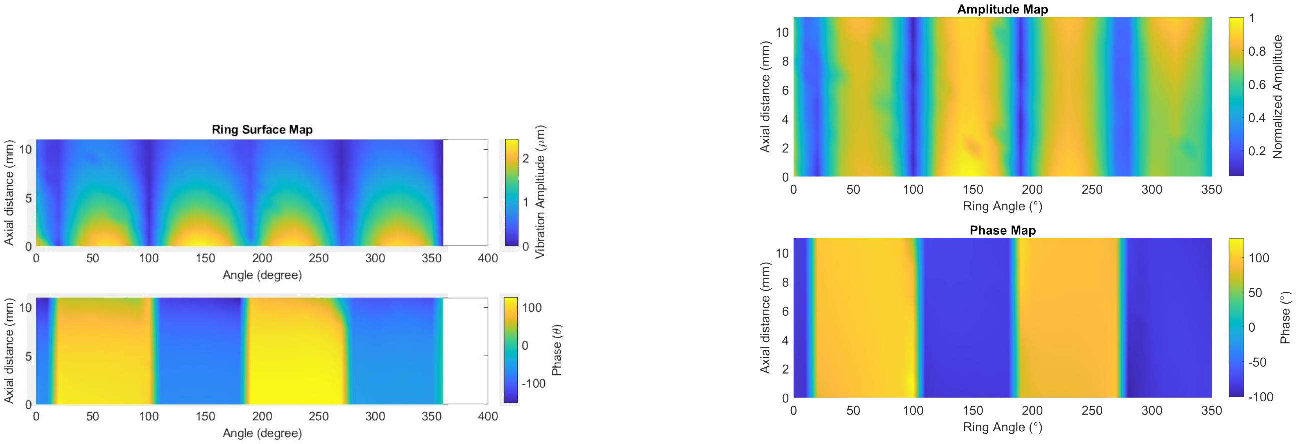

(a)

(b)

Fig. 22: (a) mode shape measurements with wires on one side (b) mode shape measurements with wires on either side

APPENDIX III
BROKEN PIEZO REPLACEMENT

Even though great care is taken with processing, soldering, and utilizing the piezos and completed rings, piezos remain fragile, and the epoxy step includes some potential inaccuracies. The piezos used in these prototypes are high quality and undergo quality control testing, however, they are brittle and are damaged when the curie temperature is exceeded. In some cases, the insertion of the wedge system resulted in some movement, resulting in some misalignment in the finished product. Apart from errors made in the production of the rings, multiple rings were damaged in the testing process. The wires that power the piezos are fed through narrow cavities in the sidecaps, which could lead to wire seizing and breaking, this problem was later alleviated by using another type of wire. Water damage also resulted in multiple broken piezos.

Since the prototype features four piezos and a single malfunctioning or misaligned piezo reduces the effectiveness of the ring, multiple rings have had to be rebuilt. It was found that it is possible to rebuild a damaged ring by heating it in a furnace at 500° Celsius until the epoxy adhesive evaporates. After rinsing the ring in acetone, the ring is ready to be rebuilt. The heating cycle does result in some surface discoloration as shown in figure 23, but the titanium itself is not affected.

Fig. 23: The surface discolouration after the furnace

APPENDIX IV
SPLIT PIEZOS FOR INCREASED PERFORMANCE

An optional addition to the current design would be to effectively split each of the four piezos in two and rotate each slightly outwards. This would yield the result shown in figure 24, the colour indicates the phase of the applied voltage. Red piezos have an 180° phase offset from blue piezos, resulting in the same mode shape as the current prototype. This adjustment can be done without fundamental changes to the supply or production process. This orientation allows the total piezo width per quadrant to increase from $5\,\mathrm{mm}$ to $6\,\mathrm{mm}$ while reducing the mass of the titanium ring. Besides reduced mass, the lumen size is further increased, leaving more space for instruments to pass through. As the number of piezos is doubled, this redesign also necessitates doubling the number of wires that are used. This could be alleviated by grounding the piezos through the ring and perhaps soldering two adjacent in-phase piezos with the same wire.

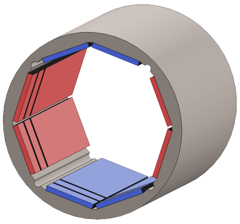

Fig. 24: A larger piezo-covered area and lumen with reduced weight through split piezos.

APPENDIX V
MINIATURIZATION

The current prototype has an outer diameter of $11\,\mathrm{mm}$, which is too large for intravenous applications. According to DEMO, the current design can be isotropically scaled down to $3\,\mathrm{mm}$ without requiring alterations to the production process. A scaled-down version with an outer diameter of $5\,\mathrm{mm}$ is proposed. Slight variations to the design are made to allow for the same thickness of piezo to be used. The vibration characteristics of the proposed design are simulated in COMSOL and the desired mode shape is achieved at $30\,722\,\mathrm{Hz}$ with a maximum at the nodal line of $1.66\,\mu\mathrm{m}$. The simulated resonant amplitude is below the desired $2\,\mu\mathrm{m}$, but higher frequencies often allow the same friction reduction to be achieved at lower amplitudes [18]. A size comparison between the current prototype and the proposed design is shown in figure 25.

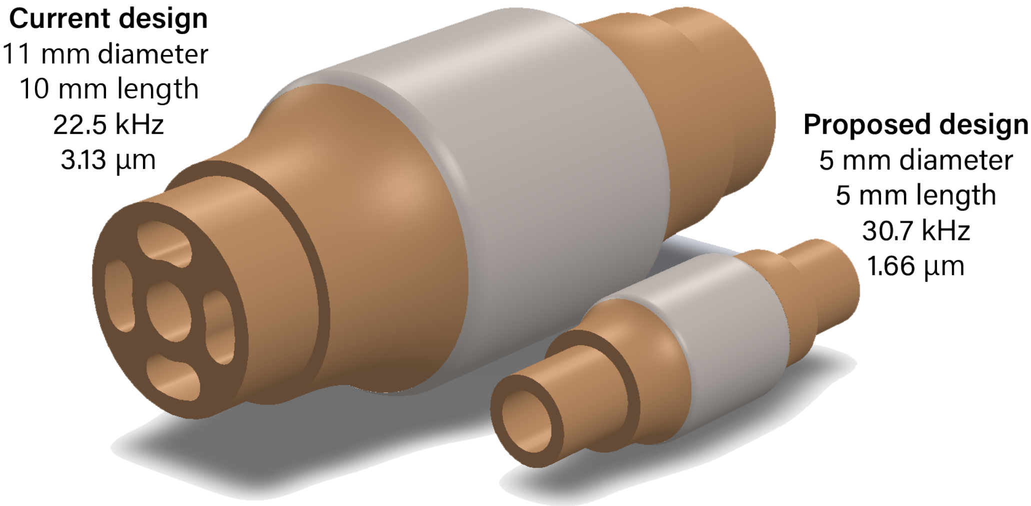

Fig. 25: Size comparison of the proposed design

Appendix VI
PROTOTYPE PRODUCTION

Production of the prototype starts with the production of the titanium ring at DEMO, a machining facility at TU Delft. The ring is made of titanium, and the machining consists of two steps. The first step is milling the fillet and chamfer on the cylinder and the second step is creating the cavity inside the ring. The cavity and its features are created using EDM. The result is shown in figure 26a.

Next is the application of the piezoelectric plates on the inner faces of the ring. The piezoelectric plates, model number ”SMPL60W5T03R112”, are cut to a length of $10\,\mathrm{mm}$. This is done by consecutive passes of a razor blade, with little applied pressure to minimize the chances of the piezo snapping in an undesired direction. The uncut piezo with a marker line at $10\,\mathrm{mm}$ is shown in figure 26b. After cutting the piezos are tested for tolerance, and piezos within $0.1\,\mathrm{mm}$ are accepted. Piezos out of tolerance are either trimmed further or discarded.

A thin layer of epoxy adhesive (3M Epoxy structural adhesive DP490) is applied to one of the inner faces of the ring, shown in figure 26c. The piezo is then put in place and gently pressed down. The entire ring is then rotated 90° to allow the next piezoelectric plate to be applied on the bottom face. This process is repeated four times, and shown in figure 27a.

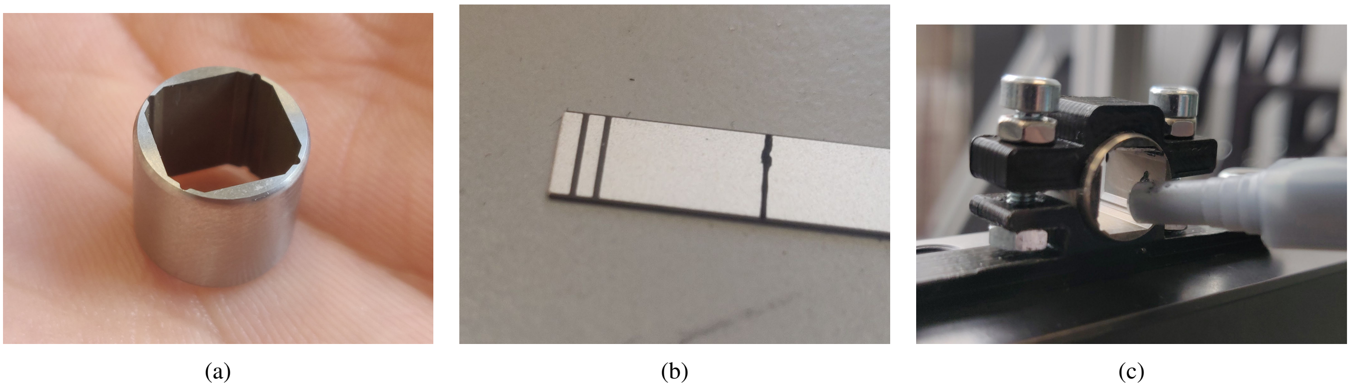
(a) (b) (c)

Fig. 26: (a) The ring after machining (b) A piezo marked for cutting (c) Application of glue

With all four piezos in place, a wedge system is inserted, which applies even pressure to the surface of the piezos. This is shown in figure 27b. Wax paper is placed between the piezos and the outer face of the wedge system to prevent the two from bonding. The wedge system is left in place for 12 hours after which the epoxy is cured.


(a) (b)

Fig. 27: (a) Two piezos in place (b) Wedge system is inserted and applies constant, equal pressure to the piezo

The wax paper and wedges are removed and some post-processing is done. $0.9\,\mathrm{mm}$ copper wires are soldered onto the top and bottom electrodes using a solder specifically made to adhere well to the silver electrode on the piezoelectric plate. The solder is ”$0.7\,\mathrm{mm}$ Lead-Free No-clean Flux Core Silver Solder 2 Oz”. These wires are attached to a wave generator through a piezo drive. This combination drives the two opposing sets of piezoelectric plates at a 180° phase shift at a tuneable voltage and frequency. This phase shift results in one set of opposing piezoelectric plates expanding, while the other set contracts, actuating the desired mode shape.